06

Features of the defect structure of nonlinear optical $LiNbO_3$:Zn:Mg single crystals

© R.A. Titov,[1] L.A. Bobreva,[1] M.V. Smirnov,[1] A.S. Krylov,[2] A.N. Vtyurin,[2] M.N. Palatnikov,[1]
I.V. Biryukova,[1] S.M. Masloboeva,[1] N.A. Teplyakova,[1] A.A. Gabain,[1] N.V. Sidorov[1]

[1]Tananaev Institute of Chemistry and Technology of Rare Elements and Minerals, Federal Research Center „Kola Scientific Center, Russian Academy of Sciences“,
184209 Apatity, Murmansk Region, Russia
[2]Kirensky Institute of Physics,
Federal Research Center „Krasnoyarsk Scientific Center, Siberian Branch, Russian Academy of Sciences“,
660036 Krasnoyarsk, Russia
e-mail: r.titov@ksc.ru

Received June 19, 2025
Revised October 15, 2025
Accepted October 18, 2025

The defect structure features of nonlinear optical double-doped $LiNbO_3$:Zn:Mg(3.91:1.01 mol.% ZnO and MgO) and $LiNbO_3$:Zn:Mg(4.48:1.04 mol.% ZnO and MgO) single crystals were studied by Raman spectroscopy, IR-spectroscopy in the region of OH-group stretching vibrations, photoinduced light scattering and laser conoscopy. The single crystals were grown by the Czochralski method from a charge of different genesis. It has been shown that the crystals are chemically and optically uniform and have the low photorefractive effect. Analysis of the behavior of the Raman spectrum band with a frequency of $120\,cm^{-1}$ has been shown that the $LiNbO_3$:Zn:Mg(3.91:1.01 mol.% ZnO and MgO) crystal has a more perfect cation sublattice. Bands ($3498-3548\,cm^{-1}$) corresponding to the stretching vibrations of hydrogen atoms in the hydroxyl groups of the Zn_{Nb}^{3-}–OH and Mg_{Li}^{+}–Mg_{Nb}^{3-}–OH complex defects have been detected in the IR-spectrum of the $LiNbO_3$:Zn:Mg(4.48:1.04 mol.%ZnO and MgO) crystal. These lines are shifted to the long-wave region of the spectrum. This fact indicates the passage of the concentration threshold in $LiNbO_3$:Zn:Mg(4.48:1.04 mol.% ZnO and MgO) crystal, when the zinc concentration increases from 3.91 mol.% to 4.48 mol.%, and the magnesium concentration increases from 1.01 mol.% to 1.04 mol.%.

Keywords: : Lithium niobate, double doping, OH–groups, point and complex defects, Raman spectroscopy, laser conoscopy, photoinduced light scattering.

DOI: 10.61011/TP.2026.02.62883.152-25

Introduction

Miscellaneous functional materials based on ferroelectric lithium niobate single crystal ($LiNbO_3$, LN) are currently much in demand. This single crystal has high acousto-optical, electro-optical, nonlinear-optical coefficients, photorefractive effect („optical damage“), wide transparency window from 0.25 to 5.5 μm and, thus, can be used for creating various materials (optical materials for visible, near and mid-IR ranges, etc.) [1–9]. In accordance with phase diagram of Nb_2O_5–Li_2CO_3, lithium niobate phase (has an oxygen-octahedral structure) is characterized by a wide homogeneity region [2,3,10,11]. Its chemical formula as a variable-composition phase can be written as $LiNbO_3$:Nb,Me (where Me is an impurity metal). Physical characteristics of $LiNbO_3$ single crystal and materials are determined by stoichiometry R (where $R = [Li]/[Nb]$), specific localization of doping metal cations in the crystal and features of the crystal defect structure. Lithium niobate crystal is heterodesmic, it has different types of interactions between structural units, which are significantly different in energy: covalent interaction, electrostatic interaction and hydrogen bond. By varying single crystal growth parameters, doped mixture technique, type, concentration and combination of doping elements, physical characteristics of $LiNbO_3$ crystals can be finely adjusted.

$LiNbO_3$ crystal structure, besides oxygen octahedra O_6 connected by edges and faces [2,12], has oxygen tetrahedra O_4, which serve as compensators of deformation changes in oxygen scaffold of the crystal [13]. Oxygen octahedra contain Li^+ and Nb^{5+}, and doping metal cations. One third of octahedra are always vacant, while the rest of octahedra contain metal cations. Such structure makes it possible to dope a crystal with a wide range of various metals. The order of sequence of metal ions along the polar axis of a crystal is defined by the crystal composition and specific crystal growth techniques. As the dopant concentration in a crystal increases, concentration thresholds occur, and when these thresholds are passed, the space symmetry group of the $LiNbO_3$ lattice cell remain unchanged, but there are changes in the order of sequence of base and impurity cations along the polar axis of the crystal and lattice cell parameters [3].

Employment of $LiNbO_3$ crystals for laser conversion, modulation and generation is limited by the photorefractive effect. The photorefractive effect is followed by wave front distortion of the electromagnetic wave passing through a crystal and by photoinduced light scattering (PILS) on laser-induced defects [3,4,14]. The photorefractive effect may be reduced by introducing optical-damage-resistant metal cations into the crystal structure. These cations have a constant oxidation degree (Mg^{2+}, Zn^{2+}, In^{3+}, Sc^{3+}, Zr^{4+}, etc.) and don't change their charge state when they are exposed to light [3,4,6,15]. Such cations (ODRI — optical-damage-resistant ions[6]) improve optical-damage-resistance of $LiNbO_3$ crystals. Introducing small amounts of ODRI into a crystal doesn't lead to full suppression of the photorefractive effect. However, compositional and optical homogeneity of crystals is retained in this case, which is a critical factor of a highly advanced optical material technology. The most significant reduction of the photorefractive effect can be achieved by introducing large amounts of ODRI, near-threshold and higher, into a crystal structure. However, introduction of such concentrations of optical-damage-resistant metal cations into the crystal structure unfortunately has a negative effect on chemical and compositional homogeneity of doped crystals and also induces various point and complex structural defects in the crystal structure.

The mechanism of dopant (Me) and base element (Li, Nb) entry into the crystal structure changes when the concentration threshold is achieved [3,4,15]. Main concentration thresholds (individual) for Zn^{2+} (5.19 mol.%) and Mg^{2+} ($\approx$ 5.5 mol.%) are established in [3,4,15]. Regardless of the fact that these concentration thresholds (of Mg and Zn) in single-doped crystals are known and their manifestation in formation of the primary and secondary (defect) structural features of $LiNbO_3$:Zn and $LiNbO_3$:Mg structures has been also investigated, features of concentration threshold (and magnitudes) manifestation in $LiNbO_3$:Zn:Mg crystals are currently insufficiently investigated. This especially refers to small (nonbasic) concentration thresholds, which insignificantly change the defect structure state of crystals. Moreover, codoping with two optical-damage-resistant impurities can mutually strengthen their impact on physical properties of the $LiNbO_3$ crystal [16]. This offers opportunities for developing new and improving existing techniques for growing highly advanced doped $LiNbO_3$ crystals with target characteristics. Thus, the properties and performance of materials can be changed in a wider range compared with single doping by changing the concentration of two dopants and the method for dopant introduction into a crystal structure taking into account their individual effect in a wide concentration range on the crystal defect structure, photorefractive properties, and optical and compositional homogeneity. To date, some properties of the following double-doped $LiNbO_3$ single crystals have been obtained and studied:

$LiNbO_3$:Zn:Mg [17–21], $LiNbO_3$:Zn:In [16],
$LiNbO_3$:Zn:Fe [22], $LiNbO_3$:Yb:Pr [23],
$LiNbO_3$:Cr:Cu [24], $LiNbO_3$:Er:Tm [25],
$LiNbO_3$:Er:Zn [26], $LiNbO_3$:Hf:Dy [27],
$LiNbO_3$:Nd:MgO [28], $LiNbO_3$:Pr:Mg [29],
$LiNbO_3$:Zr:Dy [30], $LiNbO_3$:In:Dy [31],
$LiNbO_3$:Yb:Er [32], $LiNbO_3$:Ce:Mn [33]

etc.

Authors of [21] investigated a series of double-doped $LiNbO_3$:Mg(3.0 mol.%):Zn(1.0, 2.0 and 3.0 mol.%) crystals using the IRspectroscopy method. This study shows that the number of peaks on IR spectra of the tested crystals changes: 3482 cm^{-1} for $LiNbO_3$:Mg:Zn(3.0:1.0 mol.%) crystal; 3482 and 3533 cm^{-1} for $LiNbO_3$:Mg:Zn(3.0:2.0 mol.%) crystal; 3533 cm^{-1} for $LiNbO_3$:Mg:Zn(3.0:3.0 mol.%) crystal. Such behavior of lines with 3482 cm-1 and 3533 cm^{-1} (intensity reduction of the first one and intensity increase of the second one as the Zn concentration grows) was associated by the authors of [21] with a decrease in the concentration of Nb_{Li} defects in the $LiNbO_3$:Mg:Zn crystal.

Laser conoscopy and photoinduced light scattering methods were used in [19] to identify that homogeneously-doped $LiNbO_3$:Zn:Mg crystals (dopant is introduced in the Nb_2O_5 precursor) have high resistance to laser damage and optical homogeneity. In [20] it was shown that the features of structural ordering of the cation sublattice and the defect structure state of $LiNbO_3$:Zn:Mg(3.45:1.41 mol.%) and $LiNbO_3$:Zn:Mg(3.45:1.22 mol.%) single crystals produced using the homogeneous doping and direct doping techniques, respectively, are defined by magnesium, rather than by zinc. Therefore, it is important to carry out additional studies to investigate the features of the defect structure of $LiNbO_3$:Zn:Mg crystals, which are different in origin and contain a lower concentration of Mg cations ($\approx$ 1 mol.% MgO) and a higher concentration of Zn cations ($\approx$ 4 mol.% ZnO and higher). A closely adjacent and fixed concentration of Mg cations shall make their prevailing impact on the features of crystal defect structures less pronounced compared with Zn cations, and introduction of $LiNbO_3$:Zn:Mg $\approx$ 4 mol.% ZnO and more into the crystal structure will make it possible to „pass“ the first individual threshold. This approach will be used to examine both individual influence of these dopants and the influence of their total concentration on the features of the defect structure of $LiNbO_3$:Zn:Mg crystals.

Thus, the aim of this work is to identify the role of Zn^{2+} and Mg^{2+} and their concentrations in generation of threshold effects in $LiNbO_3$:Zn:Mg(3.91:1.01 mol.%) and $LiNbO_3$:Zn:Mg(4.48:1.04 mol.%) crystals, and the role of a doping method in generation of the features of a defect structure, optical homogeneity and photorefractive properties of double-doped $LiNbO_3$:Zn:Mg crystals using the Raman scattering spectroscopy (RS), IR spectroscopy in the OH stretching region, PILS and laser conoscopy.

1. Experimental procedure

Double-doped $LiNbO_3$:Zn:Mg crystals investigated in this work were grown from a mixture produced using different techniques. $LiNbO_3$:Zn:Mg(3.91:1.01 mol.% in crystal) single crystal was grown using the homogeneous doping technique (hereinafter referred to as LN(1)) [19], $LiNbO_3$:Zn:Mg(4.48:1.04 mol.% in crystal) was grown using the combined doping method (hereinafter referred to as LN(2)) [26]. Crystal LN(1) was grown from a homogeneously zinc- and magnesium-doped lithium niobate mixture synthesized from Nb_2O_5:Mg:Zn precursor using a technique described in [19]. Crystal LN(2) was grown from a mixture where impurities were introduced in two stages [26]: stage 1 — producing the $LiNbO_3$:Mg mixture; stage 2 — adding ZnO before the crystal growth. Previously studied crystals [19,20,34] were chosen as comparison objects in this work: stoichiometric lithium niobate single crystal $LiNbO_{3stoich}$ ($R = 1$) grown from the melt with excess $[Li_2O] = 58.6$ mol.% (hereinafter referred to as — LN_s); double-doped $LiNbO_3$:Zn:Mg(3.45:1.41 mol.%) and $LiNbO_3$:Zn:Mg(3.45:1.22 mol.%) single crystals grown using the homogeneous and combined doping technique (hereinafter referred to as LN(1') and LN(2'), respectively).

LN(1) and LN(2) (diameter — 35 mm, length of cylindrical portion — 43 mm) were grown in the [001] direction by the Czochralski method from the melt using platinum crucibles, dia 80 mm, in air on the Kristall-2 industrial growth unit. For crystal growth, the axial temperature gradient was 1 deg/mm, growth rate was 14 rpm, speed was 1.1 mm/hour, and growth rate was 1.6 mm/hour [19]. For thermoelastic stress relief, composition homogenization and achievement of unidirectional state (monodomainization process), LN(1) and LN(2) underwent a set of postgrowth heat treatments [19]. Concentration of Mg and Zn dopants in the crystals of interest was measured by the inductively coupled plasma atomic emission spectrometry using the Optima 8300 ICP-AES spectrometer and by the atomic absorption spectrometry using the „Kvant-FA" instrument [19]. Table 1 shows the concentration of dopants in plates cut from the cone (C_c) and face (C_f) of the grown crystal ingots, and the change in the concentration of dopants over the ingot length ($\Delta C_{\mathrm{Me}} = C_c - C_f$) for test samples LN(1) [19] and LN(2) and doped reference samples LN(1') and LN(2') [20].

For the purpose of study, the grown crystals were reduced to a single-domain state and then test samples were cut from the crystal ingots in the form of rectangular parallelepipeds, whose faces were thoroughly polished and edges coincided in direction with the X, Y, Z crystallographic axes (Z is the polar axis of crystal), with dimensions $8 \times 6 \times 10$ mm (Figure 1).

Conoscopic patterns by the laser conoscopy method and PILS patterns of test single crystals LN(1) and LN(2) were measured using the Nd:YAG laser (MLL-100, Changchun New Industries Optoelectronics Tech. Co. Ltd, Changchun, China) with laser wavelength of 532.0 nm, power of 1 mW and 90 mW (laser conoscopy; power density of 0.04 W/cm2 and 3.54 W/cm^2, respectively) and 160 mW (PILS; power density of 6.29 W/cm^2). For detailed drawings of original systems and experimental procedure, see [35]. Laser conoscopic patterns of LN(1) and LN(2) were obtained using 3 mm plates, PILS patterns were obtained using parallelepipeds (Figure 1). PILS and conoscopic patterns of LN(1) have been earlier studied in [19].

RS spectra of LN(1) and LN(2) were recorded in the $Y(ZZ)\overline{Y}$ and $Y(ZX)\overline{Y}$ scattering geometries. RS spectra were recorded using the T64000 spectrograph (Horiba Jobin-Yvon, type 2018-RM, Lille, France). The Spectra-Physics Excelsior 532-300-CDRH laser with $\lambda = 532.0$ nm and $P = 5$ mW was used for RS spectra excitation. All spectra were recorded with a resolution of 1.0 cm^{-1}. Spectral line FWHM accuracy was ± 2 cm^{-1}.

IR spectra of test single crystals LN(1) and LN(2) were recorded with a resolution of 0.5 cm^{-1} using the Nicolet 6700 Fourier transform spectrometer(Thermo Fisher Scientific Inc., Hillsboro, OR, USA, 2010) at room temperature. Nonpolarized IR radiation was used. Volume concentration of OH groups in the test crystals was measured using Klauer's method [36].

Table 1. Concentration (in mol.%) of dopants (Zn, Mg) in the cone and face of LN(1) [19], LN(2) and reference samples LN(1') and LN(2') [20], and change in the concentration (ΔC_{Me}) of dopants (Me–Zn, Mg) over the ingot length

Crystal	Dopant concentration, mol.%					
	Cone		Face		$\Delta C_{\mathrm{Me}} = C_c - C_f$	
	[Zn]	[Mg]	[Zn]	[Mg]	[Zn]	[Mg]
LN(1)	3.91	1.01	3.85	0.96	0.06	0.05
LN(2)	4.48	1.04	4.48	1.04	0	0
LN(1')	3.45	1.41	3.45	1.44	0	−0.03
LN(2')	3.45	1.22	3.51	1.22	−0.06	0

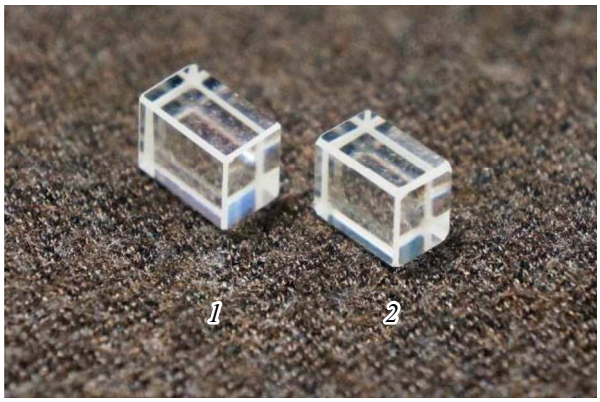

Figure 1. Single crystal samples: *1* — LN(1), *2* — LN(2).

Experimental data (RS and IR spectroscopy) of the test crystals was processed and represented in LabSpec 5.5 and Origin 8.1.

2. Results and discussions

Photoinduced light scattering is the result of photorefractive effect [37]. PILS patterns of LN(1) and LN(2) are shown in Figure 2. For test crystals LN(1) and LN(2), PILS indicatrix is not expanded, only circular scattering on static structural defects is observed (Figure 2). This is indicative of a low photorefractive effect in the test crystals. The scattering pattern doesn't vary with time and maintains its round shape throughout the experiment (Figure 2). Note that PILS patterns of LN(1) and LN(2) have a set of differences. Thus, the first PILS pattern layer of LN(1) corresponding to the laser beam that has passed through the crystal has a larger diameter than the first PILS pattern layer of LN(2), indicating a stronger laser beam energy dissipation on defects within LN(2) (Figure 2).

Laser conoscopy method was used to control optical quality of LN(1) and LN(2). The conoscopic patterns have circular symmetry where the integrity of a black „Maltese cross" is maintained in the center of the field of vision, and isochromes look like concentric circles with their center in the optical axis emergence point (Figure 3). This suggests that the samples are optically homogeneous and have good optical quality. However, note that conoscopic patterns of LN(1) have a set of features (Figure 3): when the radiation power is 1 mW, signs of anomalous optical biaxiality are observed and are partially exhibited in the form of a vertical shift of conoscopic pattern fragments. These distortions decrease in the conoscopic pattern of LN(1) recorded at a higher laser power (Figure 3). This may be associated with „healing" of defects as the laser power increases. Additionally, as the laser power increases, anomalies in the form of pairwise joining of isochromes occur on the lower right arm of the „Maltese cross" in the conoscopic pattern of LN(1) (Figure 3). Note that there is small smearing of the

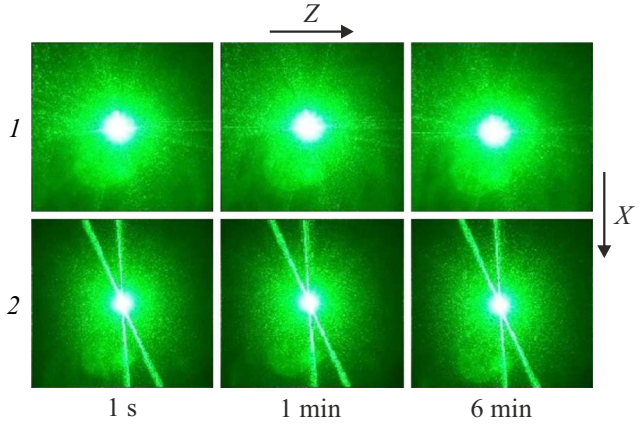

Figure 2. PILS patterns of crystals LN(1) — *1* [19] and LN(2) — *2*. $\lambda = 532$ nm, $P = 160$ mW.

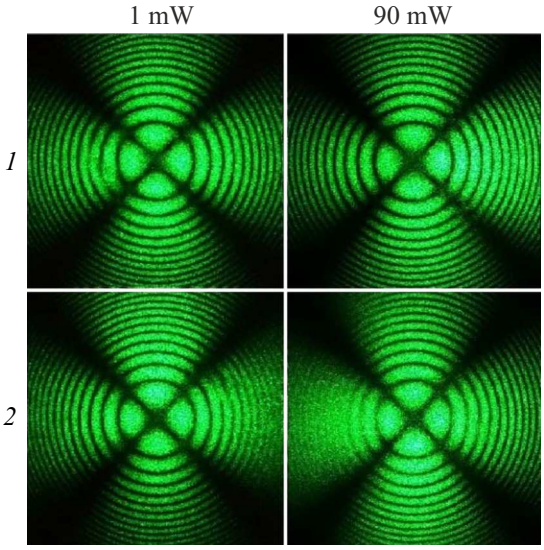

Figure 3. Conoscopic patterns of crystals LN(1) — *1* [19] and LN(2) — *2*. $\lambda = 532$ nm, $P = 1$ and 90 mW.

conoscopic pattern of LN(2) with a laser power of 90 mW, which may be caused by increasing photorefractive effect at this laser power density (Figure 3).

Anomalies found in the conoscopic patterns are indicative of a structural inhomogeneity in crystals resulting from nonuniform dopant distribution within the crystal, especially with significant concentrations of doping cations. Crystals LN(1) and LN(2) differ in high degree of chemical homogeneity (Table 1). Thus, the distortions found on the conoscopic patterns of LN(1) and LN(2) (Figure 3) and decrease in size of the first PILS pattern layer of LN(2) (Figure 2) are probably caused by rearrangement of their secondary structure due to the change in the mechanism of Zn and Mg introduction into the crystal structure near the concentration threshold. Concentration of Zn cations in the structure of LN(1) and LN(2) is close to or higher than (3.91 mol.% and 4.48 mol.% (Table 1)) the concentration corresponding to the first individual concentration threshold (3.95 mol.% ZnO in crystal [15]). For more details of the features of structural ordering of the cation sublattice and defect structure state of crystals LN(1) and LN(2), use RS and IR spectroscopy.

Figure 4 shows RS spectra ($Y(ZX)\overline{Y}$ and $Y(ZZ)\overline{Y}$) of single crystal LN_s and crystals LN(1) and LN(2). According to the selection rules, only $E(TO)$ and $A_1(TO)$ symmetry fundamental oscillations in the $X - Y$ plane and along the Z axis, respectively, shall be displayed in the specified scattering geometries [3,38]. Frequencies and FWHM of the primary spectral lines are shown in Tables 2 and 3. When processing the spectra, additional lines, the origin of which is not discussed in this work, were added to achieve maximum overlapping of the theoretical and experimental envelopes.

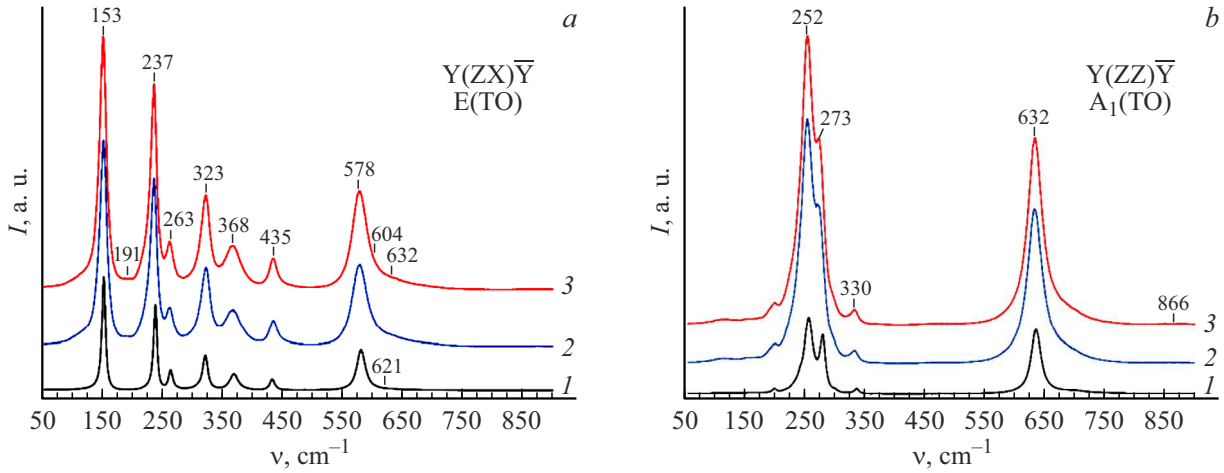

Figure 4. RS spectra of nominally pure single crystal LN_s — (*1*) [20] and single crystals LN(2) — (*2*) and LN(1) — (*3*) at $T = 293$ K in the following scattering geometries: $Y(ZX)\overline{Y}$ ($E(TO)$) — *a*; $Y(ZZ)\overline{Y}$ ($A_1(TO)$) — *b*.

Table 2. Frequencies and FWHM (v and S, cm^{-1}) of RS spectral lines of nominally pure single crystal LN_s and single crystals LN(1) and LN(2) in the $Y(ZX)\overline{Y}$ ($E(TO)$) scattering geometry at $T = 293$ K

LN_s		LN(1)		LN(2)	
v, cm^{-1}	S, cm^{-1}	v, cm^{-1}	S, cm^{-1}	v, cm^{-1}	S, cm^{-1}
153	7	152	11	153	12
–	–	190	9	191	9
239	7	237	10	237	11
264	8	263	13	263	14
322	10	323	15	323	16
370	17	368	32	368	33
433	10	435	16	435	17
581	17	578	29	578	29
–	–	605	35	604	33
621	100	–	–	–	–
–	–	633	99	632	98

Table 3. Frequencies and FWHM (v and S, cm^{-1}) of RS spectral lines of nominally pure single crystal LN_s and single crystals LN(1) and LN(2) in the $Y(ZZ)\overline{Y}$ ($A_1(TO)$) scattering geometry at $T = 293$ K

LN_s		LN(1)		LN(2)	
v, cm^{-1}	S, cm^{-1}	v, cm^{-1}	S, cm^{-1}	v, cm^{-1}	S, cm^{-1}
254	15	252	22	252	22
277	11	273	17	273	18
334	9	330	14	330	15
634	20	632	29	632	30

RS spectra of the test crystals are similar to each other (Figure 4) and correspond to the RS spectra of the lithium niobate crystal [5]. It is known that structure disordering effects contribute to the increase in FWHM of spectral lines, and, besides the structure disordering effects, the photorefractive effect additionally contributes to the increase in line intensity, which is proportional to squared derivative of polarizability of interatomic bonds participating in oscillation [3]. When analyzing RS spectra of LN(1) and LN(2), contribution of the photorefractive effect to the spectral line intensity can be neglected because laser light used for the experiments had low power (5 mW). Note that the photorefractive effect in LN(1) and LN(2) is suppressed (in accordance with the PILS data (Figure 2)). Thus, only the structure disordering effects contribute to the increase in spectral line intensity observed in transition from the spectrum of LN_s to the spectra of doped crystals (Figure 4). Intensity of most spectral lines in the given $Y(ZX)\overline{Y}$ and $Y(ZZ)\overline{Y}$ scattering geometries of LN(1) is ~ 1.2 times higher than that of spectral lines of LN(2).

An important evaluation criterion of the degree of structural disordering of the cation sublattice of doped $LiNbO_3$ crystals compared with LN_s is FWHM of spectral lines corresponding to $A_1(TO)$ oscillations of lithium, niobium and impurity cations along the polar axis of the crystal. Tables 2 and 3 show that FWHM of most spectral lines of LN(2) is larger than that for LN(1) by $\sim 1\,cm^{-1}$, which is included in the measurement error range of this spectral parameter ($\pm 2\,cm^{-1}$). Thus, RS spectroscopy in the involved $Y(ZX)\overline{Y}$ and $Y(ZZ)\overline{Y}$ scattering geometries

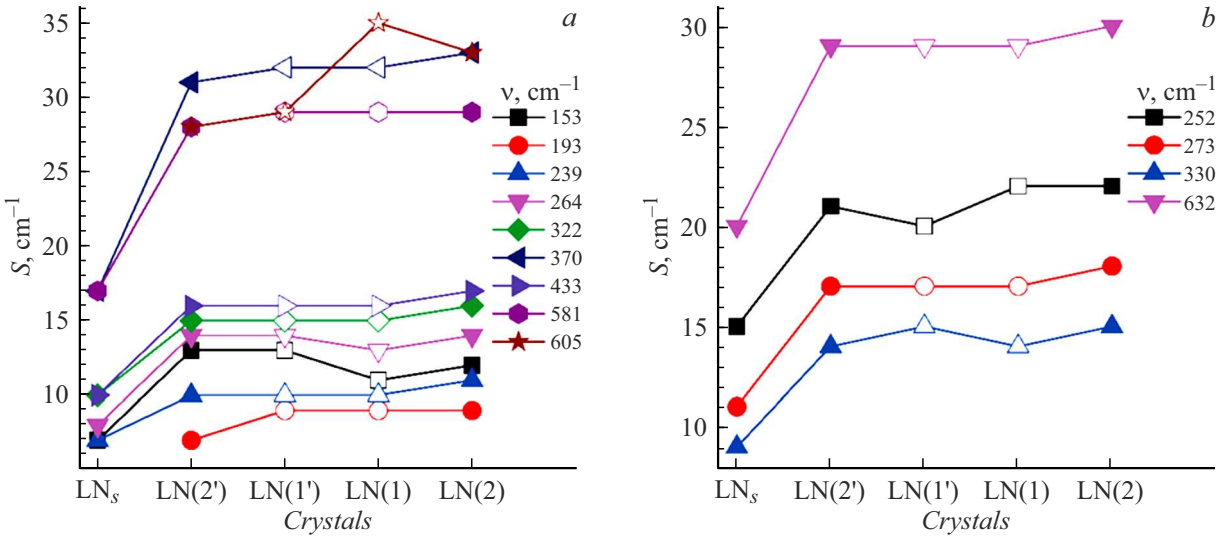

Figure 5. Concentration dependences of FWHM (S, cm^{-1}) of some spectral lines in RS spectra Y(ZX)$\overline{Y}$ — (a); Y(ZZ)$\overline{Y}$ — (b): of nominally pure crystal LN_s; single crystals LN(2') and LN(1') according to [20,34]; single crystals LN(1) and LN(2) (Table 2, 3). Crystals grown using the combined doping technique — solid symbols (except for LN_s); crystals grown using the homogeneous doping technique — empty symbols.

was not able to detect any signs of threshold effects in LN(1) and LN(2).

Figure 5 shows the concentration dependences of FWHM of some spectral lines of nominally pure crystal LN_s and single crystals LN(1) and LN(2) detected in the Y(ZX)$\overline{Y}$ and Y(ZZ)$\overline{Y}$ scattering geometries. Figure 5 shows equivalent concentration dependences of single crystals LN(2') and LN(1') [20,34]. Figure 5 shows that there are no substantial changes in the spectral line FWHM behavior. General non-monotonic increase in FWHM of most spectral lines in the series of crystals LN(2') → LN(1') → LN(1) → LN(2), which is caused by an increase in structure disordering due to an increase in the total concentration (in mol.%) of doping cations in these crystals: 4.67 → 4.86 → 4.92 → 5.52.

Intensity variation of lines with a frequency of 120 cm^{-1} corresponding to two-particle states of acoustic phonons with the total wave vector equal to zero can be used to study the signs of structural disordering effects of the cation sublattice in lithium niobate crystals with different compositions. A line with 120 cm^{-1} is found in the Y(ZZ)$\overline{Y}$ scattering geometry. However, it is absent in the RS spectrum of LN_s ($R = 1$) [3]. Figure 6 shows fragments of RS spectra of nominally pure crystal LN_s, test single crystals LN(1) and LN(2) and reference single crystals LN(1') and LN(2') [34].

Stoichiometric lithium niobate crystal has the lowest resonance interaction between two-particle states of A_1(TO) type acoustic phonons with the total wave vector equal to zero and the most low-frequency fundamental A_1(TO) type phonons — 254 cm-1 and 274 cm^{-1} [3]. Thus, crystal LN_s has no line at 120 cm^{-1} (Figure 6). For $LiNbO_{3cong}$ crystal, the line with 120 cm^{-1} is split into two lines (105 cm-1 and 118 cm^{-1}) [3,39]. This is indicative of more ordered cation sublattice of $LiNbO_{3cong}$ [3]. It is important to note that the line with 120 cm^{-1} for some $LiNbO_3$:Zn crystals is also split, but into lines with other frequencies (115 cm^{-1} and 128 cm^{-1}) [39].

In $LiNbO_3$:Zn:Mg crystals, the line with 120 cm^{-1} is either split into two lines (104 cm-1 and 116 (117) cm^{-1}) or its frequency decreases (110 cm^{-1}) (Figure 6). From LN(1') to LN(1) the intensity of the line with 104 cm^{-1} increases and the intensity of the line with 116 (117) cm^{-1} decreases (Figure 6). Thus, splitting of the line with 120 cm^{-1} typical of crystal $LiNbO_{3cong}$ [39] in the series of crystals studied in this work is only observed in samples grown using the homogeneous doping technique. This may suggest a higher degree of structural perfection of the cation sublattice of LN(1') and LN(1). However, from LN(2) to LN(2') the intensity of the line with 110 cm^{-1} increases in the given spectral region (Figure 6). Thus, in terms of RS spectroscopy, the homogeneous doping technique is preferable for doping lithium niobate crystals with two metal „optical-damage-resistant“ impurities.

As mentioned above, the RS spectroscopy was not able to detect a clear manifestation of threshold effects in LN(1) and LN(2) caused by a near-threshold or higher concentration for single doping with Zn cations. However, manifestation of threshold effects in the test crystals was detected using the IR spectroscopy in the OH^- stretching region. Figure 7, a shows IR spectra of single crystals LN(1) and LN(2). The spectrum of LN_s has 3465, 3468, 3479 and 3488 cm^{-1} bands [20]. FWHM of these bands in the IR spectrum of LN_s [20] is considerably lower than in the spectra of LN(1) and LN(2), which is indicative of larger disordering of hydrogen atom localization in the doped crystal structure (Table 4, Figure 7, a). Bands in the fre-

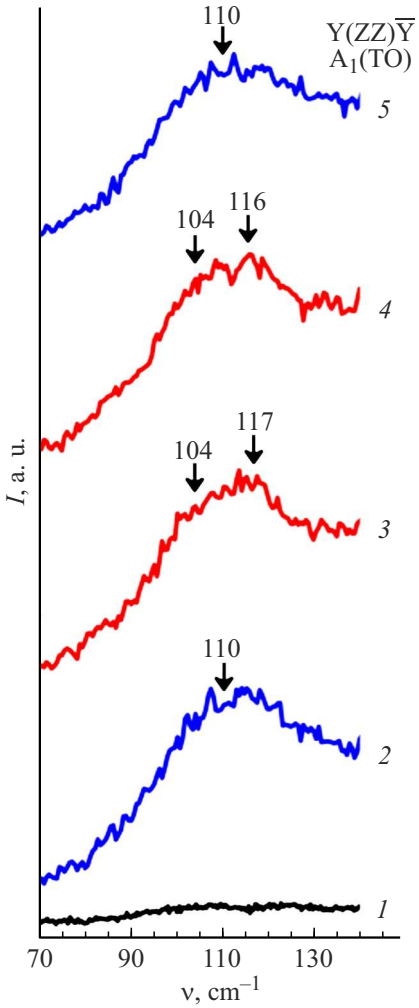

Figure 6. RS spectra fragment of nominally pure crystal LN_s — *1*, single crystals LN(2') — *2* and LN(1') — *3* (according to [34]), and single crystals LN(1) — *4* and LN(2) — *5* in the Y(ZZ)$\overline{Y}$ scattering geometry.

quency range of $3460 - 3489\,cm^{-1}$ are associated with the presence of complex defects in the crystal structure [40,41]. According to the Li vacancy compensation model, the $LiNbO_{3cong}$ lattice has ~ 1 mol.% Nb_{Li}^{4+} and ~ 4 mol.% V_{Li}^{-} [40,42]. Moreover, Zn^{2+} and Mg^{2+} contribute to distortion of the oxygen-octahedral MeO_6 clusters of the $LiNbO_3$:Zn:Mg crystal structure because their ion radii (0.74 and 0.72 Å [43]) differ from those of Nb^{5+} and Li^{+} (0.64 and 0.76 Å [43]). It is important to note that electrooptical properties of $LiNbO_3$ crystals are determined by deformation and polarizability of MeO_6 clusters (Me — Li, Nb, impurity cation) [44,45].

The shape and position of bands on the IR spectra directly depend on stoichiometry R and concentration of doping impurities in the crystal. IR spectrum of LN(2) has a frequency shift to the long-wavelength spectrum region (3498, 3505, 3512, 3528, 3535 and $3548\,cm^{-1}$) (Figure 7, *a*). Changes in the IR spectrum are observed

Table 4. Intensities and FWHM of lines (υ and S, cm^{-1}; T, a. u.) corresponding to OH^{-} stretching in IR spectra and concentration of OH^{-} groups ($C(OH^{-})$, $\cdot 10^{17}\,cm^{-3}$) of single crystals LN(1) and LN(2)

Crystals	υ, cm^{-1}	T, a. u.	S, cm^{-1}	$C(OH^{-})$, cm^{-3}
LN(1)	3470	6.29	16.72	$2.14 \cdot 10^{17}$
	3482	11.15	13.53	
	3491	6.93	12.84	
	3500	1.44	11.24	
LN(2)	3498	0.41	8.90	$2.33 \cdot 10^{17}$
	3505	0.95	9.27	
	3512	4.20	12.76	
	3528	9.00	13.21	
	3535	13.26	11.08	
	3548	0.29	6.91	

in the frequency range of $3490 - 3550\,cm^{-1}$, which reflects the change in the process of dopant entry into the crystal structure (Figure 7, *a*). Such frequency shift to the long-wavelength region is caused by formation of complex defects [41,46]. As shown in [3,15], Zn^{2+} cations occupy niobium octahedra and form Zn_{Nb} point defects usually when the main threshold is exceeded (5.19 mol.% in crystal). In the IR spectra of $LiNbO_3$:Zn crystals ($C_{Zn} > 6.76$ mol.% in melt [15]), lines with ~ 3500, 3520 and $3527\,cm^{-1}$ are detected [47]. These lines probably occur because $LiNbO_3$:Zn crystals have $Zn_{Nb}^{-3}OH$ complex defects. With this in mind, it can be assumed that three lines with 3505, 3512 and $3528\,cm^{-1}$ (Table 4, Figure 7, *b*) indicate that point defects are formed in the structure of LN(2) Zn_{Nb}^{3-}.

In [48], it was shown that the IR spectrum of $LiNbO_3$:Mg(5.29 mol.%) crystal has two lines with ~ 3526 and $3535\,cm^{-1}$. These two lines in the IR spectrum of $LiNbO_3$:Mg(5.29 mol.%) crystal are attributed to formation of Mg_{Li}^{+}–Mg_{Nb}^{3-}–OH complex defect in the crystal structure [48]. Thus, the line with $3535\,cm^{-1}$ detected in the IR spectrum of LN(2) (Table 4, Figure 7, *b*) can be caused by the presence of the above-mentioned complex defect in the structure of this crystal. Note also that the line with $3528\,cm^{-1}$ (Table 4) of LN(2) can be caused by formation of Zn_{Nb}^{3-}–OH complex defect ($\sim 3527\,cm^{-1}$ [47]) in the crystal structure as well as of Mg_{Li}^{+}–Mg_{Nb}^{3-}–OH complex defect($\sim 3526\,cm^{-1}$ [48]). With this in mind, it can be assumed that the line with $3528\,cm^{-1}$ (Table 4) in the IR spectrum of LN(2) corresponds to a complex defect containing both Zn and Mg (for example, Mg_{Li}^{+}–Mg_{Nb}^{3-}–OH, Zn_{Li}^{+}–Mg_{Nb}^{3-}–OH, Mg_{Li}^{+}–Zn_{Nb}^{3-}–OH or Zn_{Li}^{+}–Zn_{Nb}^{3-}–OH).

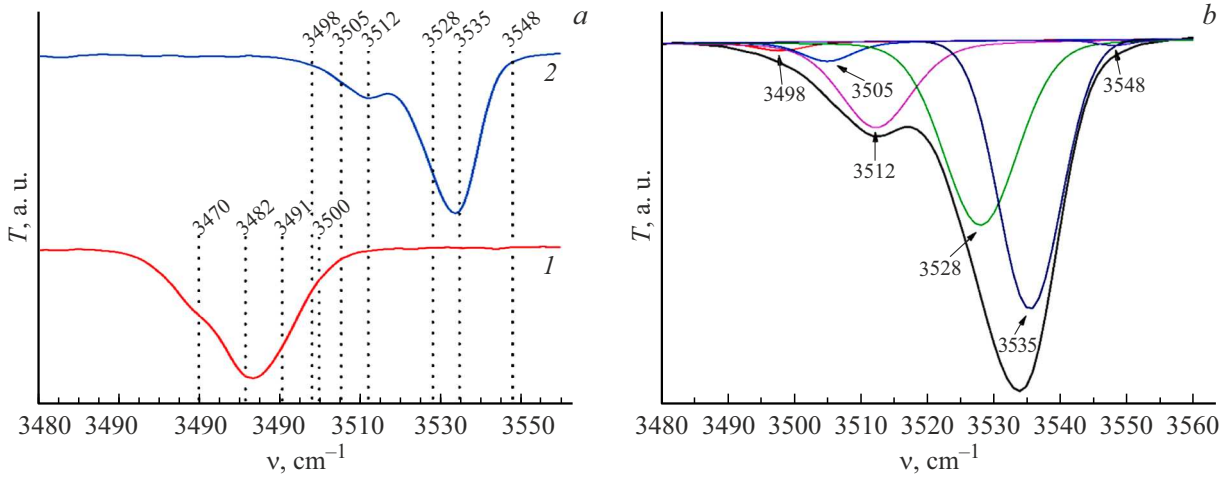

Figure 7. IR spectra (a) in the OH^- stretching region of LN(1) — *1* and LN(2) — *2*, and decomposition of the IR spectrum of LN(2) into components (b).

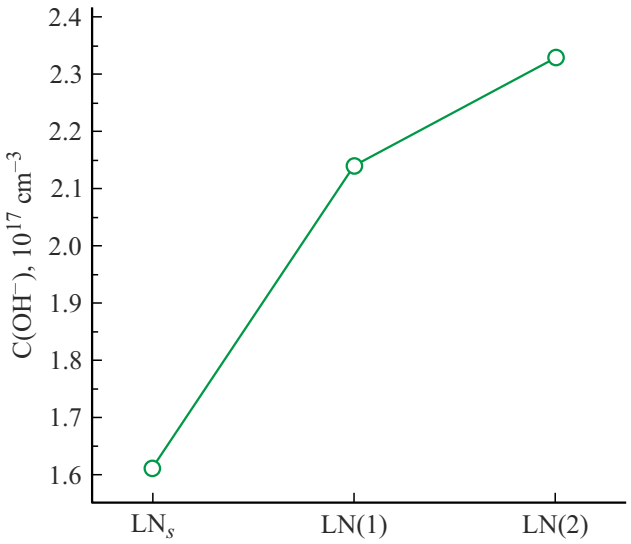

Figure 8. Concentration of OH^- groups ($C(OH^-)$, $10^{17}\,cm^{-3}$) in single crystals LN_s [20] and LN(1) and LN(2).

Note that the IR spectrum of LN(2) has no bands in the frequency range of $3460-3489\,cm^{-1}$ that are responsible for the change in stoichiometry in the crystal (Figure 7, a). But these bands are present in the IR spectra of $LiNbO_3$:Zn crystals [47] grown from melts with zinc concentration higher than the concentration threshold (~ 6.76 mol.% [15]). According to the results of X-ray diffraction analysis [15], Nb_{Li} defects are detected in these crystals. LN(2) likely has no Nb_{Li} point structural defects. This assumption is in good agreement with data from [21] concerning a decrease in the concentration of Nb_{Li} defects in the crystal $LiNbO_3$:Mg:Zn(3.0:3.0 mol.%).

It can be seen from the calculation of the volume concentration of OH^- groups using Klauer's method [36] that their concentration grows gradually as the total concentration of doping impurities increases (Figure 8, Table 4). The smallest number of OH^- groups is specific to single crystal LN_s [20] where the number of Nb_{Li}^{4+} point defects is minimum, and the largest number is specific to LN(2). Consequently, LN_s has the minimum number of negatively charged point defects (V_{Li}) forming the V_{Li}–OH complex defect.

Structural homogeneity and ion composition (ion complexes and clusters) of the melt are quite complex, even when nominally pure $LiNbO_{3cong}$ is grown [49,50]. According to [51], lithium niobate crystals are grown by means of sequential addition of ion complexes of the melt in the „melt-crystal" boundary layer. Concentration of Zn^{2+} in the test crystals is approximately four times higher than the concentration of Mg^{2+}. Therefore, Zn^{2+}, as cations having a higher concentration, in LN(2) define the localization of Mg^{2+} in oxygen octahedra O_6 of the LN(2) lattice. Zinc-defined localization of Mg^{2+} in LN(2) lattice forms the defect structure of the LN(2) cation sublattice and features of distortion of oxygen-octahedral MeO_6 clusters. This is confirmed by the presence of bands with 3528 and $3535\,cm^{-1}$ in the IR spectrum of LN(2) (Figure 7, b). Contribution to the first band is associated with Mg cations ($3526\,cm^{-1}$ [48]) and Zn cations ($3527\,cm^{-1}$ [47]), contribution to the second band is associated only with Mg cations ($3535\,cm^{-1}$ [48]). Note that the band envelope in the IR spectrum of $LiNbO_3$:Mg(5.29 mol.%) crystal is distinctly split into two bands (3526 and $3535\,cm^{-1}$) [48], while the envelope of the main band of LN(2) containing components with 3528 and $3535\,cm^{-1}$ (Figure 7) is solid. The absence of an „arm" on this band ($3535\,cm^{-1}$, Figure 7, b) of LN(2) may be attributed to the additional contribution of complex defects containing Zn^{2+}.

It can be concluded that proximity of ion radii ($r(Zn) = 0.74$ Å and $r(Mg) = 0.72$ Å [43]) of dopants and considerable (5.52 mol.%) total concentration of Zn and Mg in LN(2) preclude from exhaustively speaking about

individual concentration thresholds in the case of double doping technique. It would more correctly to conclude that there is a „common" concentration threshold (≈ 5.5 mol.% ZnO and MgO). Actually, lines caused by Zn_{Nb}^{3-}–OH and Mg_{Li}^{+}–Mg_{Nb}^{3-}–OH complex defects were detected in the IR spectrum of LN(2). In the case of single doping, the above-mentioned defects are displayed at higher concentrations in a crystal. Zn(4.68 and 6.5 mol.% [47]) and Mg(5.29 mol.% [48]).

Conclusion

The Czochralski method was used to grow double-doped $LiNbO_3$:Zn:Mg (3.91:1.01 mol.%) and $LiNbO_3$:Zn:Mg (4.48:1.04 mol.%) single crystals from a mixture of different origin, and comprehensive study of structural perfection and photorefractive properties of the crystals were carried out in comparison with nominally pure stoichiometric single crystal LN_s and $LiNbO_3$:Zn:Mg(3.45:1.41 mol.%) and $LiNbO_3$:Zn:Mg(3.45:1.22 mol.%) single crystals. It is shown that $LiNbO_3$:Zn:Mg(3.91:1.01 mol.%) and $LiNbO_3$:Zn:Mg (4.48:1.04 mol.%) crystals are optically homogeneous, have high degree of chemical homogeneity and low photorefractive effect.

In the series of $LiNbO_3$:Zn:Mg(3.45:1.22 mol.%) →
$LiNbO_3$:Zn:Mg(3.45:1.41 mol.%) →
$LiNbO_3$:Zn:Mg(3.91:1.01 mol.%) →
$LiNbO_3$:Zn:Mg(4.48:1.04 mol.%)

crystals, as the total concentration of Zn and Mg (in mol.%: $4.67 \rightarrow 4.86 \rightarrow 4.92 \rightarrow 5.52$) grows, there is the increase in crystal defects manifested in the increase in FWHM of most lines in the RS spectra. By the change in frequency and intensity of the line with 120 cm^{-1} and by splitting into two components with 104 and 116 (117) cm^{-1}, it was found that $LiNbO_3$:Zn:Mg(3.45:1.41 mol.%) and $LiNbO_3$:Zn:Mg(3.91:1.01 mol.%) crystals have a more perfect cation sublattice compared with crystals grown using the combined doping technique.

Analysis of the IR spectra of $LiNbO_3$:Zn:Mg (3.91:1.01 mol.%) and $LiNbO_3$:Zn:Mg (4.48:1.04 mol.%) crystals detected the display of threshold effects. These effects are induced by the total concentration of doping Zn and Mg cations (≈ 5.5 mol.%) in the $LiNbO_3$:Zn:Mg(4.48:1.04 mol.%) crystal and are displayed as a shift of bands to the long-wavelength region of the IR spectrum (3498, 3505, 3512, 3528, 3535 and 3548 cm^{-1}, respectively). Analysis of IR spectra of the $LiNbO_3$:Zn:Mg(4.48:1.04 mol.%) crystal and single-doped crystals has shown that Zn^{2+}-defined localization of Mg^{2+} in the double-doped crystal lattice determines the crystal's defect structure. The obtained data suggests that in the case of double doping with Zn^{2+} and Mg^{2+}, it is more correctly to imply „common" concentration threshold, which is defined by the main concentration threshold of magnesium.

Funding

The study was performed with partial financial support of research and development projects of young scientists provided by the government of the Murmansk region (№ 35 as of January 31, 2025) and under the state assignment of the Ministry of Science and Higher Education of the Russian Federation Reg. No. FMEZ-2025-0055).

Conflict of interest

The authors declare no conflict of interest.

References

[1] R.S. Weis, T.K. Gaylord. Appl. Phys. A, **37**, 191 (1985). DOI: 10.1007/BF00614817
[2] A.M. Prokhorov, Yu.S. Kuz'minov. *Physics and chemistry of crystalline lithium niobate* (Adam Hilger, NY., 1990)
[3] N.V. Sidorov, T.R. Volk, B.N. Mavrin, V.T. Kalinnikov. *Niobat litiya: defekty, fotorefraktsiya, kolebatelny spektr, polyaritony* (Nauka, M., 2003) (in Russian).
[4] T. Volk, M. Wöhlecke. *Lithium Niobate. Defects, Photorefraction and Ferroelectric Switching* (Springer, Berlin, 2008)
[5] M.D. Fontana, P. Bourson. Appl. Phys. Rev., **2** (4), 040602 (2015). DOI: 10.1063/1.4934203
[6] O. Sánchez-Dena, S.D. Villalobos-Mendoza, R. Farías, C.D. Fierro-Ruiz. Crystals, **10** (11), 990 (2020). DOI: 10.3390/cryst10110990
[7] K. Chen, Y. Zhu, Z. Liu, D. Xue. Molecules, **26** (22), 7044 (2021). DOI: 10.3390/molecules26227044
[8] C. Guanyu, L. Nanxi, D.N. Jun, L. Hong-Lin, Z. Yanyan, H.F. Yuan, Y.T.L. Lennon, Y. Yu, L. Ai-Qun, J.D. Aaron. Adv. Photonics, **4** (3), 034003 (2022). DOI: 10.1117/1.AP.4.3.034003
[9] L. Kovács, G. Corradi. Crystals, **11** (11), 1356 (2021). DOI: 10.3390/cryst11111356
[10] L.O. Svaasand, M. Eriksrud, G. Nakken, A.P. Grand. J. Cryst. Growth., **22** (3), 230 (1974). DOI: 10.1016/0022-0248(74)90099-2
[11] H.M. O'Bryan, P.K. Gallagher, C.D. Brandle. J. Am. Ceram. Soc., **68** (9), 493 (1985). DOI: 10.1111/j.1151-2916.1985.tb15816.x
[12] H.D. Megaw. Acta Cryst., **7** (2), 187 (1954). DOI: 10.1107/s0365110x54000527
[13] D. Xue, K. Kitamura, J. Wang. Opt. Mater., **23** (1−2), 399 (2003). DOI: 10.1016/S0925-3467(02)00326-9
[14] Y. Kong, F. Bo, W. Wang, D. Zheng, H. Liu, G. Zhang, R. Rupp, J. Xu. Adv. Mater., **32** (3), 1806452 (2019). DOI: 10.1002/adma.201806452
[15] M.N. Palatnikov, N.V. Sidorov, O.V. Makarova, I.V. Biryukova. *Fundamental'nye aspekty tekhnologii silno legirovannykh kristallov niobata litiya* (KNTs RAN, Apatity, 2017) (in Russian).
[16] K. Kasemir, K. Betzler, B. Matzas, B. Tiegel, T. Wahlbrink, M. Wöhlecke, B. Gather, N. Rubinina, T. Volk. J. Appl. Phys., **84** (9), 5191 (1998). DOI: 10.1063/1.368769
[17] G. Xu, J. Zhu, B. Xiao, X. Yang, X. Wang. Cryst. Res. Technol., **31** (2), K20 (1996). DOI: 10.1002/crat.2170310226
[18] X. Yang, G. Xu, H. Li, J. Zhu, X. Wang. Cryst. Res. Technol., **31** (4), 521 (1996). DOI: 10.1002/crat.2170310418

[19] S.M. Masloboeva, I.V. Biryukova, M.N. Palatnikov, N.A. Teplyakova. Russ. J. Inorg. Chem., **65** (6), 924 (2020). DOI: 10.1134/S0036023620060108
[20] R.A. Titov, M.V. Smirnov, L.A. Bobreva, N.A. Teplyakova, M.N. Palatnikov, I.V. Biryukova, S.M. Masloboeva, A.S. Krylov, A.N. Vtyurin, N.V. Sidorov. Inorg. Mater. Appl. Res., **16** (2), 278 (2025). DOI: 10.1134/S2075113324701648
[21] M.H. Li, Y.H. Xu, W.S. Xu, C.X. Liu, W.L. Zhang, Z.S. Shao. Ferroelectr., **264** (1), 273 (2001). DOI: 10.1080/00150190108008581
[22] X.H. Zhen, H.T. Li, Z.J. Sun, S.J. Ye, L.C. Zhao, Y.H. Xu. Mater. Lett., **58** (6), 1000 (2004). DOI: 10.1016/j.matlet.2003.08.005
[23] T. Bodziony, S.M. Kaczmarek, J. Hanuza. J. Alloys Compd., **451** (1–2), 240 (2008). DOI: 10.1016/j.jallcom.2007.04.189
[24] Y. Guo, L. Liu, D. Liu, S. Deng, Y. Zhi. Appl. Opt., **44** (33), 7106 (2005). DOI: 10.1364/ao.44.007106
[25] T. Bodziony. Opt. Mater., **31** (2), 149 (2008). DOI: 10.1016/j.optmat.2008.02.006
[26] I.V. Biryukova, R.A. Titov, N.A. Teplyakova, I.N. Efremov, M.N. Palatnikov. Tech. Phys., **69** (7), 1912 (2024). DOI: 10.1134/S1063784224070089
[27] L. Dai, S. Yang, R. Chen, C. Liu, X. Han, Y. Shao. J. Lumin., **217**, 116773 (2020). DOI: 10.1016/j.jlumin.2019.116773
[28] X. Chen, H. Qin, F. Wang, D. Wang, Q. Liu, Y. Cheng, F. Liang, Y. Sang, H. Yu, H. Liu, H. Zhang. Opt. Express, **33** (5), 9897 (2025). DOI: 10.1364/OE.555269
[29] J. Liu, A. Liu, Y. Chen, X. Tu, Y. Zheng. Physica B, **624**, 413419 (2022). DOI: 10.1016/j.physb.2021.413419
[30] L. Dai, L. Zhang, H. Wang, N. Lai. Cryst. Res. Technol., **59** (6), 2300255 (2024). DOI: 10.1002/crat.202300255
[31] L. Dai, Y. Shunxiang. Mater. Res. Express, **12** (3), 036302 (2025). DOI: 10.1088/2053-1591/adc173
[32] X. Tian, Q. Qi, B. Hou, Y. Qian. Inorg. Chem. Commun., **157**, 111389 (2023). DOI: 10.1016/j.inoche.2023.111389
[33] L. Galambos, S.S. Orlov, L. Hesselink, Y. Furukawa, K. Kitamura, S. Takekawa. J. Cryst. Growth., **229** (1–4), 228 (2001). DOI: 10.1016/S0022-0248(01)01128-9
[34] R.A. Titov, M.V. Smirnov, A.S. Krylov, A.N. Vtyurin, I.V. Biryukova, S.M. Masloboeva, N.V. Sidiriv, M.N. Palatnikov. *Tez. dokl. XIV-iy Mezhdunarodnoy konferentsii po fotonike i informatsionnoy optike* (M., Rossiya, 2025), s. 513 (in Russian).
[35] N.V. Sidorov, O.Yu. Pikul', N.A. Teplyakova, M.N. Palatnikov. *Lazernaya konoskopiya i fotoindutsirovannoe rasseyanie sveta v issledovaniyakh svoystv nelineyno-opticheskogo monokristalla niobata litiya* (Izd-vo RAN, M., 2019) (in Russian).
[36] S. Klauer, M. Wöhlecke, S. Kapphan. Phys. Rev. B, **45** (6), 2786 (1992). DOI: 10.1103/PhysRevB.45.2786
[37] V.A. Maksimenko, A.V. Syuy, Yu.M. Karpets. *Fotoindutsirovannye protsessy v ktistallakh niobata litiya* (Fizmatlit, M., 2008) (in Russian)
[38] S. Sanna, S. Neufeld, M. Rüsing, G. Berth, A. Zrenner, W.G. Schmidt. Phys. Rev. B, **91** (22), 224302 (2015). DOI: 10.1103/PhysRevB.91.224302
[39] N.V. Sidorov, M.N. Palatnikov, A.A. Yanichev, R.A. Titov, O.V. Makarova. Tech. Phys., **62** (3), 417 (2017). DOI: 10.1134/S1063784217030215
[40] N. Lyi, K. Kitamura, F. Izumi, J.K. Yamamoto, T. Hayashi, H. Asano, S. Kimura. J. Solid State Chem., **101** (2), 340 (1992). DOI: 10.1016/0022-4596(92)90189-3
[41] K. Lengyel, Á. Péter, L. Kovács, G. Corradi, L. Pálfalvi, J. Hebling, M. Unferdorben, G. Dravecz, I. Hajdara, Zs. Szaller, K. Polgár. Appl. Phys. Rev., **2** (4), 040601 (2015). DOI: 10.1063/1.4929917
[42] J. Blümel, E. Born, T. Metzger. J. Phys. Chem. Solids., **55** (7), 589 (1994). DOI: 10.1016/0022-3697(94)90057-4
[43] R.D. Shannon. Acta Crystallographica, A, **32**, 751 (1976). DOI: 10.1107/s0567739476001551
[44] M.D. Fontana, K. Laabidi, B. Jannot, M. Maglione, P. Jullien. Solid State Commun., **92** (10), 827 (1994). DOI: 10.1016/0038-1098(94)90322-0
[45] F. Abdi, M. Aillerie, P. Bourson, M.D. Fontana, K. Polgar. J. Appl. Phys., **84** (4), 2251 (1998). DOI: 10.1063/1.368290
[46] J.M. Cabrera, J. Olivares, M. Carrascosa, J. Rams, R. Müller, E. Diéguez. Adv. Phys., **45** (5), 349 (1996). DOI: 10.1080/00018739600101517
[47] N.V. Sidorov, L.A. Bobreva, M.N. Palatnikov, O.V. Makarova. Inorg. Mater., **55** (7), 698 (2019). DOI: 10.1134/S0020168519070173
[48] N.V. Sidorov, L.A. Bobreva, N.A. Teplyakova, M.N. Palatnikov, O.V. Makarova. Opt. i spektr., **127** (9), 460 (2019) (in Russian). DOI: 10.21883/OS.2019.09.48203.93-19
[49] S. Uda, W.A. Tiller. J. Cryst. Growth., **121** (1–2), 155 (1992). DOI: 10.1016/0022-0248(92)90185-L
[50] H. Kimura, H. Koizumi, T. Uchida, S. Uda. J. Cryst. Growth., **311** (6), 1553 (2009). DOI: 10.1016/j.jcrysgro.2008.09.178
[51] S. Uda, K. Shimamura, T. Fukuda. J. Cryst. Growth., **155** (3–4), 229 (1995). DOI: 10.1016/0022-0248(95)00231-6

Translated by E.Ilyinskaya